Average field-aligned ion velocity over the EISCAT radars

Yamazaki, Y[1]., M.J. Kosch[1,2,3], Y. Ogawa[4,5]

Physics Dept., Lancaster University, Lancaster LA1 4YB, UK.

Now at GFZ German Research Centre for Geosciences, Potsdam, Germany (yamazaki@gfz-potsdam.de)

[1]Department of Physics, Lancaster University, Lancaster LA1 4YB, UK

[2]South African National Space Agency, Hermanus 7200, South Africa

[3]University of Western Cape, Bellville 7535, South Africa

[4]National Institute of Polar Research, Tachikawa 190-8518, Japan

[5]Department of Polar Science, School of Multidisciplinary Sciences, SOKENDAI

This article has been accepted for publication and undergone full peer review but has not been through the copyediting, typesetting, pagination and proofreading process, which may lead to differences between this version and the Version of Record. Please cite this article as doi: 10.1002/2017JA023974

Abstract.

Long-term measurements by the European Incoherent Scatter (EISCAT) radars at Tromsø (69.6°N, 19.2°E) and Svalbard (78.2°N, 16.0°E) are used to determine the climatology of the field-aligned ion velocity in the F-region ionosphere (175–475 km) at high latitudes. The average ion velocity is calculated at various altitudes and times of day. The magnitude of the average field-aligned ion velocity is on the order of 10 m/s, similar to previous results at middle and low latitudes. The results obtained for the two radars are in good agreement. During daytime the direction of the average field-aligned ion velocity changes from downward to upward around 350 km, while during nighttime it is upward at all heights. The reversal height of the daytime field-aligned ion velocity depends on solar activity. It is elevated by more than 100 km during high solar flux periods compared to low solar flux periods. The Thermosphere Ionosphere Electrodynamics General Circulation Model (TIE-GCM) reproduces the main features of the field-aligned ion velocity climatology. The simulation results suggest that the plasma pressure gradient force and gravity force play a dominant role for the daytime field-aligned ion motion. The height pattern of the field-aligned ion velocity tends to be preserved in different solar activity conditions at constant pressure surfaces,

(Graduate University for Advanced Studies), Tachikawa, 190-8518, Japan

but not at constant altitudes, which explains the observed dependence on solar activity. During nighttime, the effect of the neutral wind dominates the field-aligned ion velocity.

1. Introduction

The ion velocity is an important parameter to represent the dynamic state of the ionosphere. In the F-region ionosphere, the ion motion perpendicular to the geomagnetic field can be approximated as follows [e.g., *Richmond*, 1995a]:

$$\mathbf{V}_{i\perp} = \frac{\mathbf{E} \times \mathbf{B}}{B^2}, \tag{1}$$

where $\mathbf{V}_i$ is the ion velocity with the subscript $\perp$ denoting the component perpendicular to the geomagnetic field $\mathbf{B}$, and $\mathbf{E}$ is the electric field. At high latitudes where the magnetic inclination is large, the $\mathbf{E} \times \mathbf{B}$ drift governs the horizontal motion of the plasma, with the typical magnitude of several 100 m/s [e.g., *Ruohoniemi and Baker*, 1998]. At middle and low latitudes, the average ion drift velocity is much smaller, with the typical magnitude of several 10 m/s [e.g., *Blanc and Amayene*, 1979; *Buonsanto et al.*, 1993; *Fejer*, 1993; *Oliver et al.*, 1993]. The $\mathbf{E} \times \mathbf{B}$ drift plays an important role at the magnetic equator in the vertical transport of plasma across the geomagnetic field [e.g., *Fejer et al.*, 1979; 2008]. The climatology of the perpendicular ion velocity ($\mathbf{V}_{i\perp}$) has been extensively studied for the purpose of calculating the electric field for both mid-low latitudes [e.g., *Richmond et al.*, 1980, 1995a; *Heelis and Coley*, 1993] and high latitudes [e.g., *Weimer*, 1995, 2005; *Cousins and Shepherd*, 2010].

The ion motion parallel to the geomagnetic field, on the other hand, can be derived from the balance of these three forces: the ion-neutral frictional force,

$$\mathbf{F} = m_i \nu_{in} \left(\mathbf{V}_{i\parallel} - \mathbf{U}_{n\parallel} \right), \tag{2}$$

the gravity force,

$$\mathbf{G} = -m_i \mathbf{g}_{\parallel}, \tag{3}$$

and the plasma pressure gradient force,

$$\mathbf{P} = \frac{k}{N_e}\frac{\partial}{\partial \mathbf{s}}\left\{N_e\left(T_i + T_e\right)\right\}. \tag{4}$$

Here m_i is the ion mass, ν_{in} is the ion-neutral collision frequency, $\mathbf{U}_{n\parallel}$ is the neutral wind velocity in the geomagnetic field direction, $\mathbf{g}_{\parallel}$ is the gravitational acceleration along the geomagnetic field, k is Boltzmann's constant, N_e is the plasma density, $\mathbf{s}$ is the unit vector in the geomagnetic field direction, and T_i and T_e are the ion and electron temperatures, respectively. The force balance leads to the following expression for the field-aligned ion velocity [e.g., *Dang et al.*, 2015]:

$$\mathbf{V}_{i\parallel} = \mathbf{U}_{n\parallel} - \frac{1}{\nu_{in}}\left[-\mathbf{g}_{\parallel} + \frac{k}{N_e m_i}\frac{\partial}{\partial \mathbf{s}}\left\{N_e\left(T_i + T_e\right)\right\}\right], \tag{5}$$

The second term on the right-hand side is often referred to as the ambipolar diffusion velocity ($\mathbf{V}_D$). That is,

$$\mathbf{V}_{i\parallel} = \mathbf{U}_{n\parallel} - \mathbf{V}_D. \tag{6}$$

At low and middle latitudes, the magnitude of the average field-aligned ion velocity is on the order of 10 m/s [*Fejer*, 1993; *Oliver et al.*, 1993].

Unlike the perpendicular ion velocity ($\mathbf{V}_{i\perp}$), the climatology of the parallel ion velocity ($\mathbf{V}_{i\parallel}$) has not been well studied. *Fejer* [1993] presented the seasonal climatology of the field-aligned ion velocity at Arecibo (18.3°N, 66.8°W) for solar maximum and solar minimum conditions. They noted a strong influence of solar activity on the field-aligned ion velocity, but the mechanism was not addressed. In the present study, we examine the climatology of the field-aligned ion velocity at high latitudes based on long-term data from the European Incoherent Scatter (EISCAT) radars.

Previous studies involving the EISCAT field-aligned ion velocity measurements focused on strong upward ion flows (several 100 m/s) that are either naturally caused [e.g., *Jones et al.*, 1988; *Winser et al.*, 1988; *Wahlund et al.*, 1992; *Fujii et al.*, 2002; *Ogawa et al.*, 2011; *Cohen et al.*, 2015] or artificially induced by high-power high-frequency radio waves [e.g., *Kosch et al.*, 2010, 2014]. Such ion upflow "events" in the topside ionosphere are possibly associated with the outflow of ionospheric ions to the magnetosphere [e.g., *Norqvist et al.*, 1998; *Wu et al.*, 2000; *Coley et al.*, 2003], which is considered to be a significant source of the magnetospheric plasma [e.g., *Yau and André*, 1997]. From this perspective, a number of statistical studies have been conducted for large-velocity ion upflow events based on EISCAT measurements. Ion upflow events are often defined by the occurrence of an upward field-aligned ion velocity greater than an arbitrary threshold value (typically 100 m/s) [*Keating et al.*, 1990; *Foster et al.*, 1998; *Endo et al.*, 2000; *Liu et al.*, 2001; *Buchert et al.*, 2004; *Ogawa et al.*, 2009, 2011]. Unlike those studies, we do not put an emphasis on large-velocity ion upflow events. Rather, we aim to determine and understand the background, or climatological state of the field-aligned ion velocity at high latitudes. Besides EISCAT radar data, we also use a first-principles model of the upper atmosphere, the Thermosphere Ionosphere Electrodynamics General Circulation Model (TIE-GCM), to facilitate the interpretation of the results.

2. Data and Model

2.1. Incoherent scatter radars

The EISCAT 930 MHz ultra-high-frequency (UHF) radar [*Rishbeth and van Eyken*, 1993] is located in Tromsø, Norway (69.6°N, 19.2°E). The radar site is in the auroral region; the quasi-dipole latitude [*Richmond*, 1995b] is 67°N. The radar operation started

in 1981, and hence the UHF data now extend over 30 years [*Ogawa et al.*, 2014]. The ionospheric parameters N_e, T_i, T_e, and $\mathbf{V}_{i\|}$ are derived from the radar spectra using the Grand Unified Incoherent Scatter Design and Analysis Package (GUISDAP) [*Lehtinen and Huuskonen*, 1996]. The analysis is made with an integration time of 5 min, and the ionospheric parameters are obtained for the height range 175–475 km. We use the observations made in the geomagnetic field-parallel direction during 1981–2014.

We also use ion velocity measurements from the EISCAT Svalbard Radar (ESR) [*Wannberg et al.*, 1997], located at 78.2°N, 16.0°E, in Longyearbyen, Svalbard, Norway. The quasi-dipole latitude is 76°N, thus the radar is usually in the polar cap. The radar data are obtained from the 42-m dish antenna that is fixed in the field-aligned position. Radar operations with the 42-m dish antenna started in 1999. The ESR data during 1999–2014 are processed basically in the same way as the UHF data.

To give a brief overview of the radar data coverage, we present in Figure 1 monthly averages of (a) N_e, (b) T_i, (c) T_e, and (e) $\mathbf{V}_{i\|}$ at 375 km altitude observed by the UHF radar during daytime (0800–1600 LT) under quiet geomagnetic conditions (geomagnetic activity index $K_p \leq 2^+$). In Figures 1a–1c and 1e–1f, the red dots indicate the monthly mean values with the error bars representing the standard deviation. The blue lines show the least squares fit of the equation $C = a + bF_{10.7}$ to the monthly mean ionospheric data (N_e, T_i, T_e, or $\mathbf{V}_{i\|}$), representing the solar cycle influence. Here, $F_{10.7}$ is the monthly solar activity index shown in Figure 1g, and a and b are the fitting coefficients evaluated for each ionospheric parameter. The solar-cycle influence on N_e and T_i is clearly seen in Figures 1a and 1b, which is well known from previous studies [e.g., *Schunk and Sojka*, 1982; *Cai et al.*, 2007; *Ogawa et al.*, 2014]. The solar-cycle effect is less obvious in the T_e data (Figure

1e), but the tendency exists that the electron temperature is lower during solar maximum than solar minimum. The lower electron temperature during solar maximum is considered to be due to enhanced electron density, which increases the cooling rate of the electron gas [*Schunk and Nagy*, 1978; *Zhang and Holt*, 2004]. In Figure 1d, the monthly mean electron temperature is plotted as a function of month. A mathematical representation of the seasonal variation in the form $D = \sum_{k=0}^{2} \{a_k \cos(kM/12) + b_k \sin(kM/12)\}$ is also shown, where M is the month, and a_k and b_k (k=0,1,2) are the fitting coefficients. It is seen from Figures 1c and 1d that the seasonal effect dominates over the solar-cycle effect in the month-to-month variability of T_e.

Figure 1e reveals that the daytime field-aligned ion velocity at 375 km is under an influence of solar activity. It can be seen that the monthly mean field-aligned ion motion is often upward during solar minimum and downward during solar maximum. Figure 1f shows the same as Figure 1e but for the ESR data. The field-aligned ion velocity at Svalbard depends on solar activity in a similar manner as the field-aligned ion velocity at Tromsø. Large variability in the $\mathbf{V}_{i\|}$ data can be inferred from the size of error bars. The statistical significance of the solar-cycle effect on $\mathbf{V}_{i\|}$ will be discussed later in Section 3.

2.2. TIE-GCM

The TIE-GCM is a physics-based model of the upper atmosphere, developed at the National Center for Atmospheric Research (NCAR) [*Richmond et al.*, 1992; *Qian et al.*, 2014]. We use version 2.0 of the model with the horizontal resolution of $5^\circ \times 5^\circ$ in latitude and longitude and the vertical resolution of half a scale height. The TIE-GCM solves continuity, momentum, and energy equations for the coupled ionosphere-thermosphere system [*Dickinson et al.*, 1984; *Roble et al.*, 1988] with electrodynamics calculated in a

realistic geomagnetic field configuration [*Richmond*, 1995b]. The model uses a log-pressure coordinate system, where constant-pressure surfaces are defined as Z=ln (P_0/P). Here, P is the pressure in hPa and P_0 is the reference pressure 5×10^{-7} hPa. The lower and upper boundaries of the model are Z=-7 (∼97 km) and Z=7 (450–650 km depending on solar activity), respectively. The geometric height is also calculated at each grid point in order to enable direct comparison with EISCAT radar data.

The high-latitude electric field is prescribed using the empirical model by *Heelis et al.* [1982] with the fixed hemispheric power of 20.6 GW and cross polar cap potential of 35.8 kV, which represents a geomagnetically quiet condition roughly corresponding to K_p=1^+. The simulations are run for two solar activity conditions; one with $F_{10.7}$=190 solar flux unit, or SFU (1 SFU = 10^{-22}Wm^{-2}Hz^{-1}) and the other with $F_{10.7}$=70 SFU, representing high and low solar flux conditions, respectively. For each case, these four seasonal conditions are considered: the December solstice with the day of year DoY=355, the March equinox with DoY=80, the June solstice with DoY=172, and the September equinox with DoY=264. All the simulations are run until a diurnally reproducible state is established. Following *Dang et al.* [2015], the field-aligned ion velocity is computed using Eq. (5) with the assumption of the dominance of atomic oxygen ions in the F-region ionosphere.

3. Results

3.1. Field-aligned ion velocity climatology from EISCAT radars

We use the EISCAT radar measurements of the field-aligned ion velocity to determine the climatology of $\mathbf{V}_{i\|}$. The average field-aligned velocity was calculated at different heights and different times of day using the corresponding data within the range of ±150

m/s from the median value. The data outside this velocity range were excluded from averaging in order to prevent a small number of strong upflow or downflow events from dominating the results. The results we present in this paper are not sensitive to the choice of this velocity range. A test we performed revealed that the $\mathbf{V}_{i\|}$ climatologies derived from the measurements within the range of ±150 m/s and ±500 m/s from the median value are substantially the same.

Figures 2a and 2e show the average field-aligned ion velocity over Tromsø during 1981–2014 for $K_p \leq 2^+$ and $K_p \geq 3^-$ conditions, respectively. The results reveal that the direction and magnitude of the average field-aligned ion velocity depend on UT and altitude. The magnitude is typically on the order of 10 m/s. The UT-altitude pattern is consistent between the lower and higher geomagnetic activity cases. For instance, during 0600–1600 UT (corresponding to 0700–1700 LT, thus daytime), the average field-aligned ion motion is downward below 350 km or so, but it is upward at higher altitudes. During 2000–0200 UT (corresponding to 2100–0300 LT, thus nighttime), the average field-aligned ion motion tends to be upward independent of height. The nighttime upward ion velocity increases with increasing geomagnetic activity.

Figures 2b, 2c, and 2d display the distribution of the daytime $\mathbf{V}_{i\|}$ between 12 and 13 UT for the lower geomagnetic activity case at 400, 300, 200 km, respectively. The best-fit normal distribution curves are also shown. In each panel, the mean value (denoted as ME), standard deviation (denoted as SD), and estimated 2σ error are indicated. The data are often normally distributed, but sometimes skewed as in Figure 2b. The 2σ errors are estimated as twice the standard deviation of the mean value using the bootstrap method [*Efron*, 1981] with 3000 iterations. In theory, if the data distribution is normal,

the 2σ error equals twice the standard error ($=\frac{SD}{\sqrt{n}}$, where n is the number of observations) that corresponds to the 95% confidence interval. The 2σ error can be used to evaluate the statistical significance of the results. For example, the altitude variation of $\mathbf{V}_{i\|}$ is a few tens of m/s at 12–13 UT for the lower geomagnetic activity case, which is much greater than the 2σ error of $\sim$1 m/s presented in Figures 2b–2d. Figures 2f–2h are the same as Figures 2b–2d but for the nighttime data between 22 and 23 UT for the higher geomagnetic activity case. We noted that the variability of $\mathbf{V}_{i\|}$ tends to be greater during nighttime than daytime, and also tends to be greater for the higher geomagnetic activity case than for the lower geomagnetic activity case.

Figure 3 shows the corresponding results for Svalbard. The UT-altitude patterns (Figures 3a and 3e) are similar to the Tromsø results (Figures 2a and 2e). That is, there is a reversal in the direction of the average ion velocity from downward at lower altitudes to upward at higher altitudes. Also, the ion motion is predominantly upward during nighttime. *Buchert et al.* [2004] reported that approximately 30% of the daytime ion upflow event (>200 m/s), observed by the Svalbard radar, was accompanied by a significant downflow (>20 m/s) at lower heights. Our results suggest that the diverging field-aligned ion flow exists even in the background state.

A comparison of Figures 3b–3d with Figures 2b–2d reveals that the standard deviation (SD) of the the daytime $\mathbf{V}_{i\|}$ tends to be greater at Svalbard than at Tromsø, indicating higher variability. This could be due to the higher occurrence rate of transient events in the cusp region (thus at Svalbard), such as a flux transfer event that can cause an ion upflow [*Lockwood et al.*, 1988; *Moen et al.*, 2004]. As seen in Figures 3b and 2b, the data

distribution is slightly skewed toward the positive side in the topside ionosphere, which is also consistent with the effect of ion upflows due to transient events.

Figure 4 depicts the seasonal dependence of the average field-aligned ion velocity at (a–c) Tromsø and (g–i) Svalbard. As can be seen in the figure, the main characteristics of the ion velocity climatology are largely the same for different seasons. Nevertheless, there seem to be some systematic seasonal changes. For instance, the downward ion velocity during daytime below 350 km is greater during the winter (November–February) than during the summer (May–August). The nighttime upward ion velocity is greatest during the summer (May–August) and least during the equinox (March, April, September and October). These seasonal features are consistent at Tromsø and Svalbard. 2σ errors are calculated in the same way described earlier and the results are shown in Figures 4d–4f for Tromsø and in Figures 4j–4l for Svalbard. In either case, the average 2σ error is $\sim$2 m/s.

The solar-cycle influence is depicted in Figures 5a and 5b for Tromsø, and in Figures 5e and 5f for Svalbard. The results are presented for high solar flux periods (daily $F_{10.7}$>150 SFU) and low solar flux periods (daily $F_{10.7}$<75 SFU). The corresponding 2σ errors can be found in Figures 5c, 5d, 5g, and 5h. The average 2σ error is $\sim$2 m/s for both Tromsø and Svalbard. However, we noted large variability of $\mathbf{V}_{i\|}$ above 400 km for Tromsø and above 450 km for Svalbard for the lower solar activity case. Thus, the results at these altitudes need to be interpreted with caution.

A strong influence of solar activity can be seen in Figures 5a, 5b, 5e, and 5f. The solar activity effect is evident during daytime. That is, the altitude for the reversal from downward to upward ion motion is much higher during the high solar flux periods. This

leads to the solar-cycle change in the direction of the field-aligned ion velocity at 375 km as shown earlier in Figures 1e and 1f. The solar activity effect is not evident in the nighttime data.

3.2. Field-aligned ion velocity climatology from the TIE-GCM

We show in Figure 6 the field-aligned ion velocity based on TIE-GCM simulations. The model results are presented as the average of four seasonal runs, thus comparable with the observations in Figures 5a, 5b, 5e, and 5f. (Figures S1 and S2 in the supporting information show the TIE-GCM results for each season and each solar activity.) The TIE-GCM reproduces well the UT-altitude pattern of the field-aligned ion velocity as well as its solar activity dependence. The most significant difference between the model and data is that the TIE-GCM field-aligned ion velocity during solar minimum is too large above 350 km or so. In Figure 6, the scale range is limited from -40 to 40 m/s to facilitate comparison with the radar results. The TIE-GCM field-aligned ion velocity exceeds 200 m/s at 450 km during daytime. The overestimation of the field-aligned ion velocity at high altitudes is partly due to the neglect of helium in our calculation of the ion-neutral collision frequency. It is known that helium is an important neutral species during solar minimum at high latitudes [*Sutton et al.*, 2015]. According to our estimation, however, the inclusion of helium would increase the ambipolar diffusion velocity only by 10% or so, which cannot fully explain the difference between the model and observations. The model-data discrepancy is more likely due to the breakdown of the force-balance assumption used in the calculation of the field-aligned ion velocity. As mentioned earlier, Eq. (5) is based on the balance of ion-neutral frictional force, gravity force, and plasma

pressure gradient force, neglecting other effects, such as the frictional force associated with the field-aligned current.

4. Discussion

4.1. Solar activity dependence of the daytime field-aligned ion velocity

As described above, the altitude pattern of the daytime field-aligned ion velocity depends on solar activity. That is, the reversal height from downward to upward ion motion increases with increasing solar activity (Figures 5a, 5b, 5e, and 5f). Since the solar activity effect is well reproduced by the TIE-GCM (Figure 6), we take a closer look at the simulation results to provide insight into the mechanism. In what follows, our discussion is based on the TIE-GCM results for Tromsø, although the argument holds for the Svalbard results as well. The TIE-GCM results for Svalbard are similar to the Tromsø results, and therefore omitted to avoid repetition. It is also noted that the following discussion does not apply to the regions above 400 km under solar minimum conditions where the model-data discrepancy is particularly large.

The field-aligned ion velocity in the TIE-GCM is calculated assuming the balance of the ion-neutral frictional force ($\mathbf{F}$), gravity force ($\mathbf{G}$), and plasma pressure gradient force ($\mathbf{P}$). Figures 7a and 7b illustrate the balance of these forces at the Tromsø location at 1200 LT under high and low solar flux conditions, respectively. For the plasma pressure gradient force $\mathbf{P}$, the results derived from the Tromsø UHF radar measurements of N_e, T_i, and T_e are also presented by the dashed lines. The model-data agreement is remarkably good above 200 km. Comparison of Figures 7a and 7b with the corresponding results in Figures 6a and 6b reveals that the height pattern of the daytime field-aligned ion velocity reflects the height profile of $\mathbf{P}+\mathbf{G}$. Therefore, it can be interpreted that the daytime field-aligned

ion motion is primarily driven by **P**+**G**, and the frictional force **F** arises to counterbalance **P**+**G**.

The reversal height from downward to upward ion motion roughly corresponds to the height where **P**+**G** equals 0. Since the gravity force **G** is independent of solar activity, the solar activity dependence of the reversal height is attributable to the solar activity dependence in **P**. The question now is why the height pattern of **P** depends on solar activity.

The solar activity dependence of **P** is mainly due to the solar-cycle effect on the plasma density profile. For simplicity, we consider the height of **P**=0, which corresponds to the height of N_e peak in the $F2$ layer (or $hmF2$). The $F2$-peak height generally increases with increasing solar activity [e.g., *Buonsanto*, 1990; *Roininen et al.*, 2015], and it tends to stay at a constant pressure level in the neutral atmosphere [*Garriott and Rishbeth*, 1969; *Rishbeth and Edwards*, 1989]. The logic behind this is as follows. At F-region heights, the plasma population is dominated by O^+. The main production mechanism of O^+ is the photoionization of atomic oxygen O, while the main loss mechanism involves a reaction with molecular species M. Accordingly, the plasma density tends to vary with the ratio of the density of atomic oxygen to the density of molecular species, denoted here as [O]/[M]. On a constant pressure surface, the [O]/[M] ratio does not change with temperature, although the height of the constant pressure surface can change. For example, during high solar flux periods, enhanced solar heating leads to a thermal expansion of the neutral atmosphere, causing constant pressure surfaces to rise in altitude. As a result, the entire N_e profile shifts to higher altitudes during solar maximum compared to solar minimum. Accordingly, **P** varies with solar activity in the altitude coordinate. In the pressure

coordinate, on the other hand, the vertical profile of N_e tends to be preserved, and so does **P**. To make this point clear, we show in Figure 8 the field-aligned ion velocity climatology at Tromsø in the log-pressure coordinate system. The effect of solar activity is much less prominent in comparison with the corresponding results in Figures 6a and 6b that are presented in the geometric height coordinate system.

4.2. Upward field-aligned ion motion during nighttime

Next, we consider the average field-aligned ion velocity during nighttime. In both observations and simulations, the nighttime ion motion is mostly upward regardless of height. The force balance of **F**, **G**, and **P** during nighttime is depicted in Figure 9 (see also Figures 6a and 6b for the corresponding field-aligned ion velocity). The results reveal that **P**+**G** is downward in a wide range of heights during nighttime, while the nighttime $\mathbf{V}_{i\|}$ is mainly upward. This is different from the daytime results where the height pattern of $\mathbf{V}_{i\|}$ agrees with the height pattern of **P**+**G**. The reason for this becomes clear when the field-aligned ion velocity is divided into the contributions by neutral wind and ambipolar diffusion (Eq. 6). It can be seen from Figure 10 that the effect of an upward field-aligned neutral wind (30–40 m/s) dominates the field-aligned ion velocity during nighttime. Thus, the ion-plasma frictional force **F**, induced by the neutral wind, is considered to be the primary driver of the field-aligned ion motion during nighttime. The strong equatorward wind is responsible for the upward field-aligned wind. The equator wind forces plasmas upward along the geomagnetic field lines.

High-latitude neutral winds at F-region heights are sensitive to geomagnetic activity [e.g., *Aruliah et al.*, 1991; *Föster et al.*, 2008]. In general, the wind speed increases with geomagnetic activity owing to forcing by enhanced ion-drag and Joule heating. This ex-

plains the geomagnetic activity dependence of the field-aligned ion velocity during nighttime shown in Figure 2.

5. Conclusions

We have examined the climatology of the field-aligned ion velocity based on long-term measurements from the EISCAT radars at Tromsø (since 1981) and Svalbard (since 1999). The main results of this study may be summarized as follows:

1. The direction and magnitude of the average field-aligned ion velocity depend on UT and altitude.

2. The magnitude of the average field-aligned ion velocity is on the order of 10 m/s.

3. The field-aligned ion velocity climatologies derived for Tromsø and Svalbard are largely consistent.

4. During daytime, the direction of the average field-aligned ion velocity reverses from downward to upward around 350 km. The reversal height increases with solar activity.

5. The TIE-GCM reproduces the main features of the field-aligned ion velocity climatology at high latitudes.

6. The TIE-GCM results suggest that the plasma pressure gradient force and gravity force play a dominant role for the daytime field-aligned ion motion. The height pattern of the plasma pressure gradient force varies with solar activity because it tends to be preserved at constant plasma pressure surfaces, but not at constant altitudes. This is the reason for the solar activity dependence of the daytime field-aligned ion velocity.

7. During nighttime, the average field-aligned ion velocity is predominantly upward at all heights from 175 to 475 km. The magnitude of the nighttime field-aligned ion velocity increases with geomagnetic activity.

8. According to the TIE-GCM results, the ion-neutral frictional force induced by the equatorward neutral wind plays a dominant role for the field-aligned ion motion during nighttime.

9. There is significant model-data disagreement above 400 km under solar minimum conditions, which requires more studies.

Acknowledgments.

We are indebted to the director and staff of EISCAT for operating the facility and supplying the data. EISCAT is an international association supported by research organizations in China (CRIRP), Finland (SA), Japan (NIPR and STEL), Norway (NFR), Sweden (VR), and the United Kingdom (NERC). The EISCAT data used in the present study can be downloaded from the archive at NIPR (http://pc115.seg20.nipr.ac.jp/www/eiscatdata/). The TIE-GCM was developed by the Atmosphere Ionosphere Magnetosphere (AIM) Section of the High Altitude Observatory (HAO) at NCAR and is available at http://www.hao.ucar.edu/modeling/tgcm/. NCAR is sponsored by the National Science Foundation. The data from our TIE-GCM simulations will be made available upon request to Y.Y (yamazaki@gfz-potsdam.de). This work was supported by NERC grant NE/K01207X/1.

References

Aruliah, A. L., D. Rees, and T. J. Fuller-Rowell (1991), The combined effect of solar and geomagnetic activity on high latitude thermospheric neutral winds. Part I. Observations, *J. Atmos. Terr. Phys.*, *53*, 467–483.

Blanc, M., and P. Amayenc (1979), Seasonal variations of the ionospheric $E \times B$ drifts above Saint-Santin on quiet days, *J. Geophys. Res.*, *84*(A6), 2691–2704, doi:10.1029/JA084iA06p02691.

Buchert, S. C., Y. Ogawa, R. Fujii, and A. P. van Eyken (2004), Observations of diverging field-aligned ion flow with the ESR, *Ann. Geophys.*, *22*, 889–899.

Buonsanto, M. J. (1990), Observed and calculated $F2$ peak heights and derived meridional winds at mid-latitudes over a full solar cycle, *J. Atmos. Sol. Terr. Phys.*, *52*, 223–240.

Buonsanto, M. J., M. E. Hagan, J. E. Salah, and B. G. Fejer (1993), Solar cycle and seasonal variations in F region electrodynamics at Millstone Hill, *J. Geophys. Res.*, *98*(A9), 15677–15683, doi:10.1029/93JA01187.

Cai, H. T., S. Y. Ma, Y. Fan, Y. C. Liu, and K. Schlegel (2007), Climatological features of electron density in the polar ionosphere from long-term observations of EISCAT/ESR radar, *Ann. Geophys.*, *25*, 2561–2569, doi:10.5194/angeo-25-2561-2007.

Cohen, I. J., M. R. Lessard, R. H. Varney, K. Oksavik, M. Zettergren, and K. A. Lynch (2015), Ion upflow dependence on ionospheric density and solar photoionization, *J. Geophys. Res. Space Physics*, *120*, 10039–10052, doi:10.1002/2015JA021523.

Coley, W. R., R. A. Heelis, and M. R. Hairston, High-latitude plasma outflow as measured by the DMSP spacecraft (2003), *J. Geophys. Res.*, *108*(A12), 1441, doi:10.1029/2003JA009890.

Cousins, E. D. P., and S. G. Shepherd (2010), A dynamical model of high-latitude convection derived from SuperDARN plasma drift measurements, *J. Geophys. Res.*, *115*, A12329, doi:10.1029/2010JA016017.

Dang, T., J. Lei, X. Dou, and W. Wan (2015), Feasibility study on the derivation of the O^+-O collision frequency from ionospheric field-aligned observations, J. Geophys. Res. Space Physics, 120, 60296035, doi:10.1002/2015JA020987.

Dickinson, R. E., E. C. Ridley, and R. G. Roble (1984), Thermospheric general circulation with coupled dynamics and composition, *J. Atmos. Sci.*, *41*, 205–219.

Efron, B. Nonparametric estimates of standard error: the jackknife, the bootstrap, and other methods (1981), *Biometrika*, *68*(3), 589–59.

Endo, M., R. Fujii, Y. Ogawa, S. C. Buchert, S. Nozawa, S. Watanabe, and N. Yoshida (2000), Ion upflow and down flow at the topside ionosphere observed by the EISCAT VHF radar, *Ann. Geophys.*, *18*, 170–181, doi:10.1007/s00585-000-0170-3.

Fejer, B. G. (1993), F region plasma drifts over Arecibo: Solar cycle, seasonal, and magnetic activity effects, *J. Geophys. Res.*, *98*(A8), 13645–13652, doi:10.1029/93JA00953.

Fejer, B., D. Farley, R. Woodman, and C. Calderon (1979), Dependence of equatorial F region vertical drifts on season and solar cycle, *J. Geophys. Res.*, *84*(A10), 5792–5796, doi:10.1029/JA084iA10p05792.

Fejer, B. G., J. W. Jensen, and S.-Y. Su (2008), Quiet time equatorial F region vertical plasma drift model derived from ROCSAT-1 observations, *J. Geophys. Res.*, *113*, A05304, doi:10.1029/2007JA012801.

Foster, C., M. Lester, and J. A. Davies (1998), A statistical study of diurnal, seasonal and solar cycle variations of F region and topside auroral upflows observed by EISCAT

between 1984 and 1996, *Ann. Geophys.*, *16*, 1144–1158, doi:10.1007/s00585-998-1144-0.

Förster, M., S. Rentz, W. Köhler, H. Liu, and S. E. Haaland (2008), IMF dependence of high-latitude thermospheric wind pattern derived from CHAMP cross-track measurements, *Ann. Geophys.*, *26*, 1581–1595.

Fujii, R., S. Oyama, S. C. Buchert, S. Nozawa, and N. Matuura (2002), Field-aligned ion motions in the E and F regions, *J. Geophys. Res.*, *107*(A5), doi:10.1029/2001JA900148.

Garriott, O. K., and H. Rishbeth (1963), Effects of temperature changes on the electron density profile in the $F2$ layer, *Planet. Space Sci.*, *11*, 587–590.

Heelis, R. A., and W. R. Coley (1992), East-west ion drifts at mid-latitudes observed by Dynamics Explorer 2, *J. Geophys. Res.*, *97*(A12), 19461–19469, doi:10.1029/92JA01840.

Heelis, R. A., J. K. Lowell, and R. W. Spiro (1982), A model of the high-latitude ionospheric convection pattern, *J. Geophys. Res.*, *87*, 6339–6345, doi:10.1029/JA087iA08p06339.

Jones, G. O. L., P. J. S. Williams, K. J. Winser, M. Lockwood, and K. Suvanto (1988), Large plasma velocities along the magnetic field line in the auroral zone, *Nature*, *336*, 231.

Keating, J. G., F. J. Mulligan, D. B. Doyle, K. J. Kinser, and M. Lockwood (1990), A statistical study of large field-aligned flows of thermal ions at high-latitudes, *Planet. Space Sci.*, *9*, 1187–1201.

Kosch, M. J., Y. Ogawa, M. T. Rietveld, S. Nozawa, and R. Fujii (2010), An analysis of pump-induced artificial ionospheric ion upwelling at EISCAT, *J. Geophys. Res.*, *115*, A12317, doi:10.1029/2010JA015854.

Kosch, M. J., H. Vickers, Y. Ogawa, A. Senior, and N. Blagoveshchenskaya (2014), First observation of the anomalous electric field in the topside ionosphere by ionospheric modification over EISCAT, *Geophys. Res. Lett.*, *41*, 7427–7435, doi:10.1002/2014GL061679.

Lehtinen, M. S., and A. Huuskonen (1996), General incoherent scatter analysis and GUISDAP, *J. Atmos. Terr. Phys.*, *58*(1), 435–452.

Liu, H., S.-Y. Ma, and K. Schlegel (2001), Diurnal, seasonal, and geomagnetic variations of large field-aligned ion upflows in the high-latitude ionospheric F region, *J. Geophys. Res.*, *106*, 24651–24661, doi:10.1029/2001JA900047.

Lockwood, M., M. F. Smith, C. J. Farrugia, and G. L. Siscoe (1988), Ionospheric ion upwelling in the wake of flux transfer events at the dayside magnetopause, *J. Geophys. Res.*, *93*(A6), 5641–5654, doi:10.1029/JA093iA06p05641.

Moen, J., K. Oksavik, and H. C. Carlson (2004), On the relationship between ion upflow events and cusp auroral transients, *Geophys. Res. Lett.*, *31*, L11808, doi:10.1029/2004GL020129.

Norqvist, P., M. Andr, and M. Tyrland (1998), A statistical study of ion energization mechanisms in the auroral region, *J. Geophys. Res.*, *103*(A10), 23459–23473, doi:10.1029/98JA02076.

Ogawa, Y., S. C. Buchert, R. Fujii, S. Nozawa, and A. P. van Eyken (2009), Characteristics of ion upflow and downflow observed with the European Incoherent Scatter Svalbard radar, *J. Geophys. Res.*, *114*, A05305, doi:10.1029/2008JA013817.

Ogawa, Y., S. C. Buchert, A. Sakurai, S. Nozawa, and R. Fujii (2010), Solar activity dependence of ion upflow in the polar ionosphere observed with the European Incoherent Scatter (EISCAT) Tromsø UHF radar, *J. Geophys. Res.*, *115*, A07310,

doi:10.1029/2009JA014766.

Ogawa, Y., S. C. Buchert, I. Häggström, M. T. Rietveld, R. Fujii, S. Nozawa, and H. Miyaoka (2011), On the statistical relation between ion upflow and naturally enhanced ion-acoustic lines observed with the EISCAT Svalbard radar, *J. Geophys. Res.*, *116*, A03313, doi:10.1029/2010JA015827.

Ogawa, Y., T. Motoba, S. C. Buchert, I. Häggström, and S. Nozawa (2014), Upper atmosphere cooling over the past 33 years, *Geophys. Res. Lett.*, *41*, 5629–5635, doi:10.1002/2014GL060591.

Oliver, W. L., Y. Yamamoto, T. Takami, S. Fukao, M. Yamamoto, and T. Tsuda (1993), Middle and upper atmosphere radar observations of ionospheric electric fields, *J. Geophys. Res.*, *98*(A7), 11615–11627, doi:10.1029/93JA00503.

Qian, L., Burns, A. G., Emery, B. A., Foster, B., Lu, G., Maute, A., Richmond, A. D., Roble, R. G., Solomon, S. C. and Wang, W. (2014), The NCAR TIE-GCM, in *Modeling the Ionosphere-Thermosphere System* (eds J. Huba, R. Schunk and G. Khazanov), John Wiley & Sons, Ltd, Chichester, UK. doi: 10.1002/9781118704417.ch7

Richmond, A. D. (1995a), Ionospheric electrodynamics, in *Handbook of Atmospheric Electrodynamic*, vol. 2, edited by H. Volland, pp. 249–290, CRC Press, Boca Raton, Fla.

Richmond, A. D. (1995b), Ionospheric electrodynamics using magnetic apex coordinates, *J. Geomagn. Geoelectr.*, *47*, 191–212.

Richmond, A. D., et al. (1980), An empirical model of quiet-day ionospheric electric fields at middle and low latitudes, *J. Geophys. Res.*, *85*(A9), 4658–4664, doi:10.1029/JA085iA09p04658.

Richmond, A. D., E. C. Ridley, and R. G. Roble (1992), A thermosphere/ionosphere general circulation model with coupled electrodynamics, *Geophys. Res. Lett.*, *19*(6), 601–604, doi:10.1029/92GL00401.

Rishbeth, H., and R. Edwards (1989), The isobaric *F*2-layer, *J. Atmos. Terr. Phys.*, *51*, 321–338.

Rishbeth, H., and A. Van Eyken (1993), EISCAT: Early history and the first ten years of operation, *J. Atmos. Terr. Phys.*, *55*(4), 525–542.

Roble, R. G., E. C. Ridley, A. D. Richmond, and R. E. Dickinson (1988), A coupled thermosphere/ionosphere general circulation model, *Geophys. Res. Lett.*, *15*, 1325–1328, doi:10.1029/GL015i012p01325.

Roininen, L., M. Laine, and T. Ulich (2015), Time-varying ionosonde trend: Case study of Sodankylä hmF2 data 1957–2014, *J. Geophys. Res. Space Physics*, 120, 6851–6859, doi:10.1002/2015JA021176.

Ruohoniemi, J. M., and K. B. Baker (1998), Large-scale imaging of high-latitude convection with Super Dual Auroral Radar Network HF radar observations, *J. Geophys. Res.*, *103*(A9), 20797–20811, doi:10.1029/98JA01288.

Schunk, R. W., and A. F. Nagy (1978), Electron temperatures in the F region of the ionosphere: Theory and observations, *Rev. Geophys.*, *16*(3), 355–399, doi:10.1029/RG016i003p00355.

Schunk, R. W., and J. J. Sojka (1982), Ion temperature variations in the daytime high-latitude F region, *J. Geophys. Res.*, *87*(A7), 5169–5183, doi:10.1029/JA087iA07p05169.

Sutton, E. K., J. P. Thayer, W. Wang, S. C. Solomon, X. Liu, and B. T. Foster (2015), A self-consistent model of helium in the thermosphere, *J. Geophys. Res. Space Physics*,

120, 6884–6900, doi:10.1002/2015JA021223.

Wahlund, J.-E., H. J. Opgenoorth, I. Häggström, K. J. Winser, and G. O. L. Jones (1992), EISCAT observations of topside ionospheric ion outflows during auroral activity: Revisited, *J. Geophys. Res.*, *97*(A3), 3019–3037, doi:10.1029/91JA02438.

Wannberg, G., et al. (1997), The EISCAT Svalbard radar: A case study in modern incoherent scatter radar system design, *Radio Sci.*, *32*(6), 2283–2307, doi:10.1029/97RS01803.

Weimer, D. R. (1995), Models of high-latitude electric potentials derived with a least error fit of spherical harmonic coefficients, *J. Geophys. Res.*, *100*(A10), 1959519607, doi:10.1029/95JA01755.

Weimer, D. R. (2005), Improved ionospheric electrodynamic models and application to calculating Joule heating rates, *J. Geophys. Res.*, *110*, A05306, doi:10.1029/2004JA010884.

Winser, K. J., G. O. L. Jones, and P. J. S. Williams (1988), Large field-aligned velocities observed by EISCAT, *J. Atmos. Terr. Phys.*, *50*, 379–382.

Wu, X.-Y., J. L. Horwitz, and Y. Seo (2000), Statistical analysis of F region and topside ionospheric ion field-aligned flows at high latitudes, *J. Geophys. Res.*, *105*(A2), 2477–2494, doi:10.1029/1999JA900437.

Yau, A. W., and M. André (1997), Sources of ion outflow in the high latitude ionosphere, *Space Sci. Rev.*, *80*, 1–25, doi:10.1023/A:1004947203046.

Zhang, S.-R., and J. M. Holt (2004), Ionospheric plasma temperatures during 1976–2001 over Millstone Hill, *Adv. Space Res.*, *33*(6), 963–969.

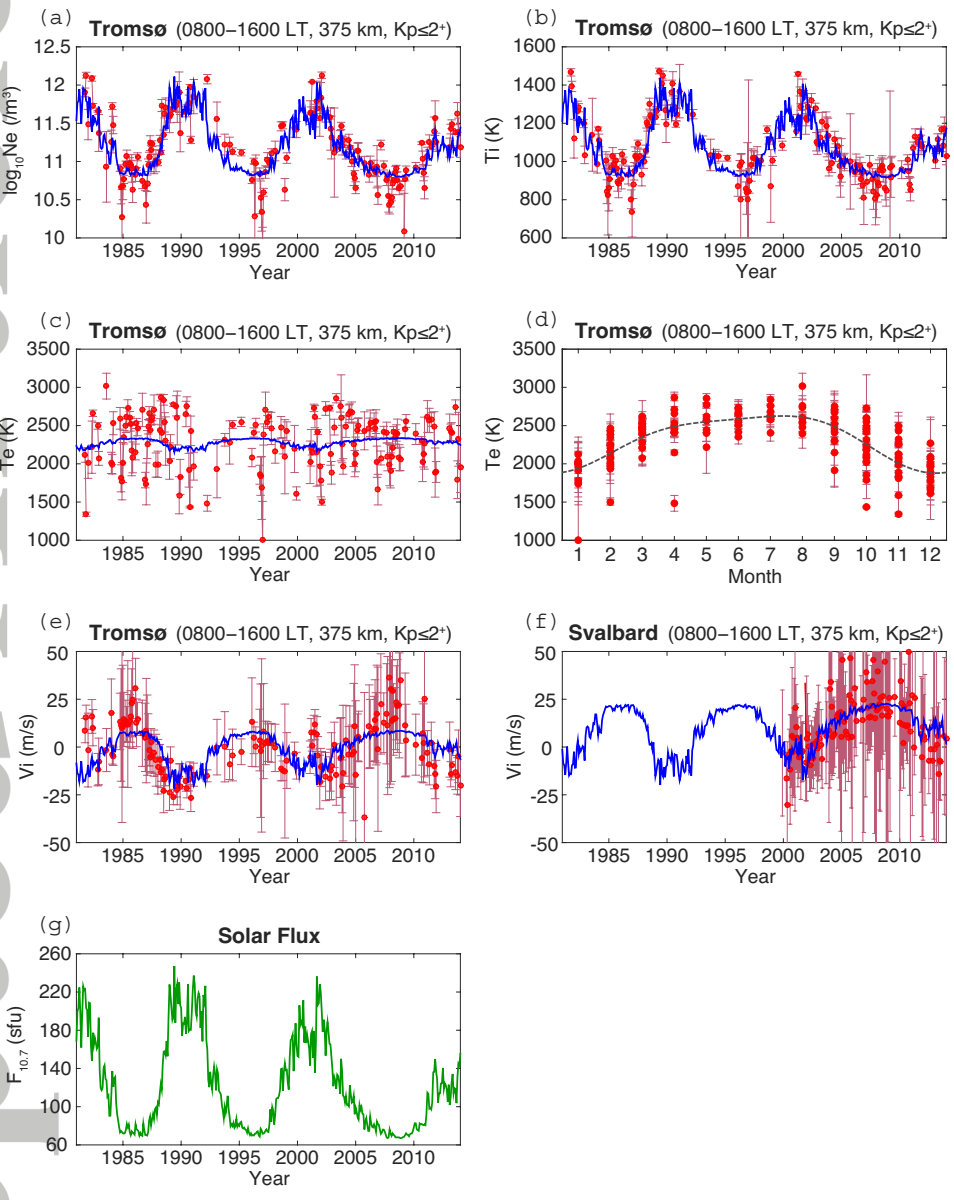

Figure 1. Time series of (a) plasma density (N_e), (b) ion temperature (T_i), (c) electron temperature (T_e), and (e) field-aligned ion velocity ($\mathbf{V}_{i\|}$, positive upward) at 375 km, obtained from the EISCAT radar at Tromsø under geomagnetically quiet conditions ($K_p \leq 2^+$) during 1981–2014. Shown are monthly averages of the daytime measurements (0800–1600 LT). The error bars represent the standard deviation, and the blue lines represent the least-squares fit of the function $C = a + bF_{10.7}$ to the corresponding ionospheric data (see text for details). (d) Seasonal variation of T_e, with the least-squares fit of the function $D = \sum_{k=0}^{2} \{a_k \cos(kM/12) + b_k \sin(kM/12)\}$ (see text for details). (f) Same as (e) except for Svalbard. (g) Monthly values of the $F_{10.7}$ index.

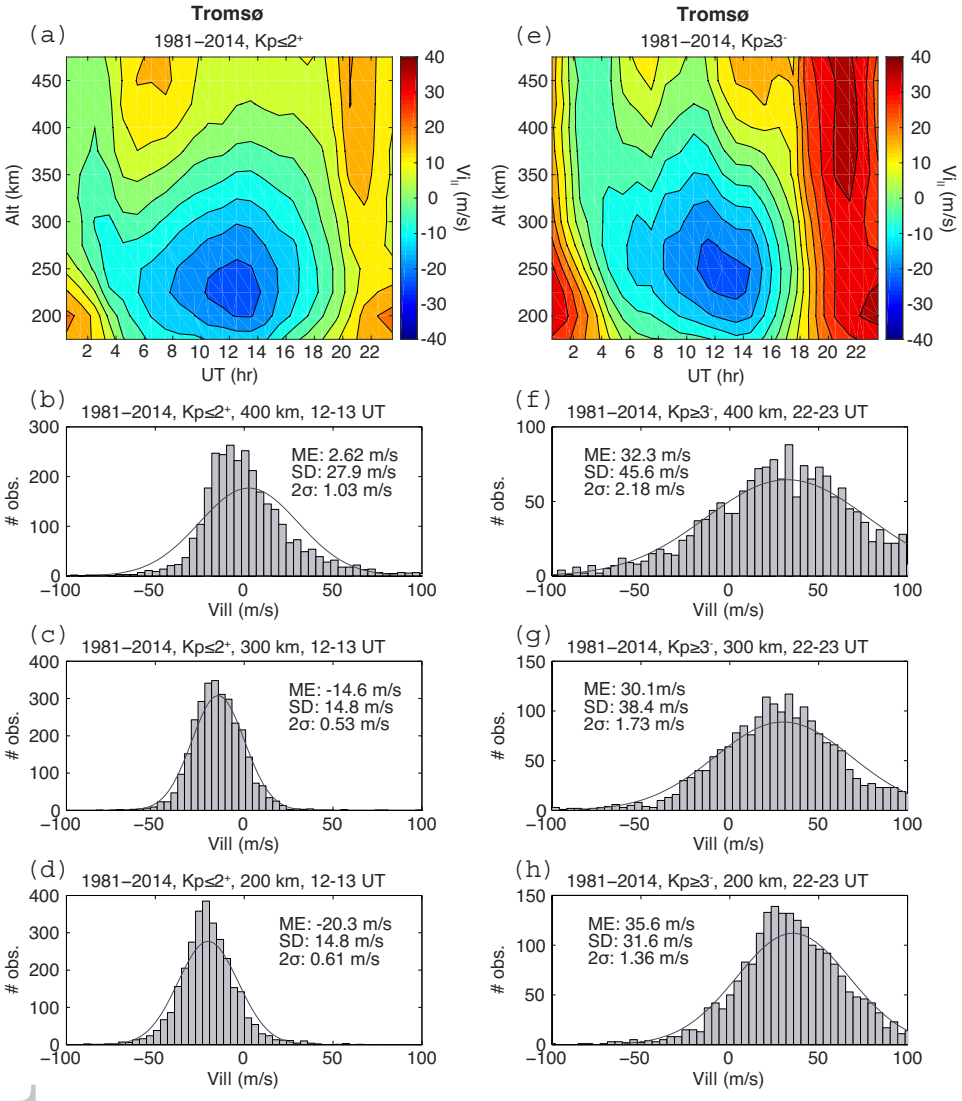

Figure 2. (a) The average field-aligned ion velocity (positive upward) at Tromsø during 1981–2014 as a function of UT and altitude for $K_p \leq 2^+$. (b–d) The distribution of $\mathbf{V}_{i\|}$ (positive upward) between 12 and 13 UT for $K_p \leq 2^+$ at 400, 300, and 200 km. (e) Same as (a) but for $K_p \geq 3^-$. (f–h) The distribution of $\mathbf{V}_{i\|}$ (positive upward) between 22 and 23 UT for $K_p \geq 3^-$ at 400, 300, and 200 km. The average standard deviations are 29.7 and 34.7 m/s for (a) and (e), respectively. The average 2σ errors are 1.26 and 1.78 m/s for (a) and (e), respectively.

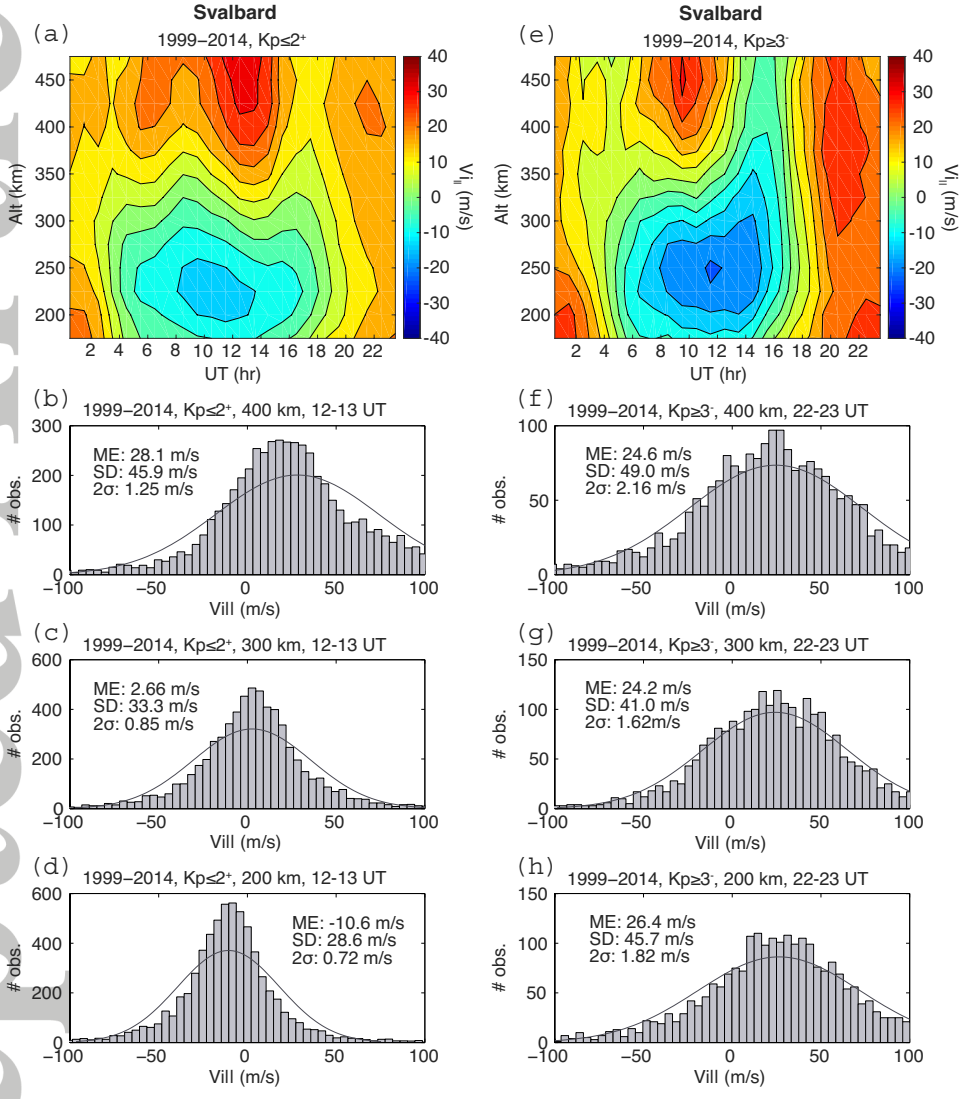

Figure 3. Same as Figure 2 except for Svalbard during 1999–2014. The average standard deviations are 37.8 and 44.5 m/s for (a) and (e), respectively. The average 2σ errors are 1.09 and 1.96 m/s for (a) and (e), respectively.

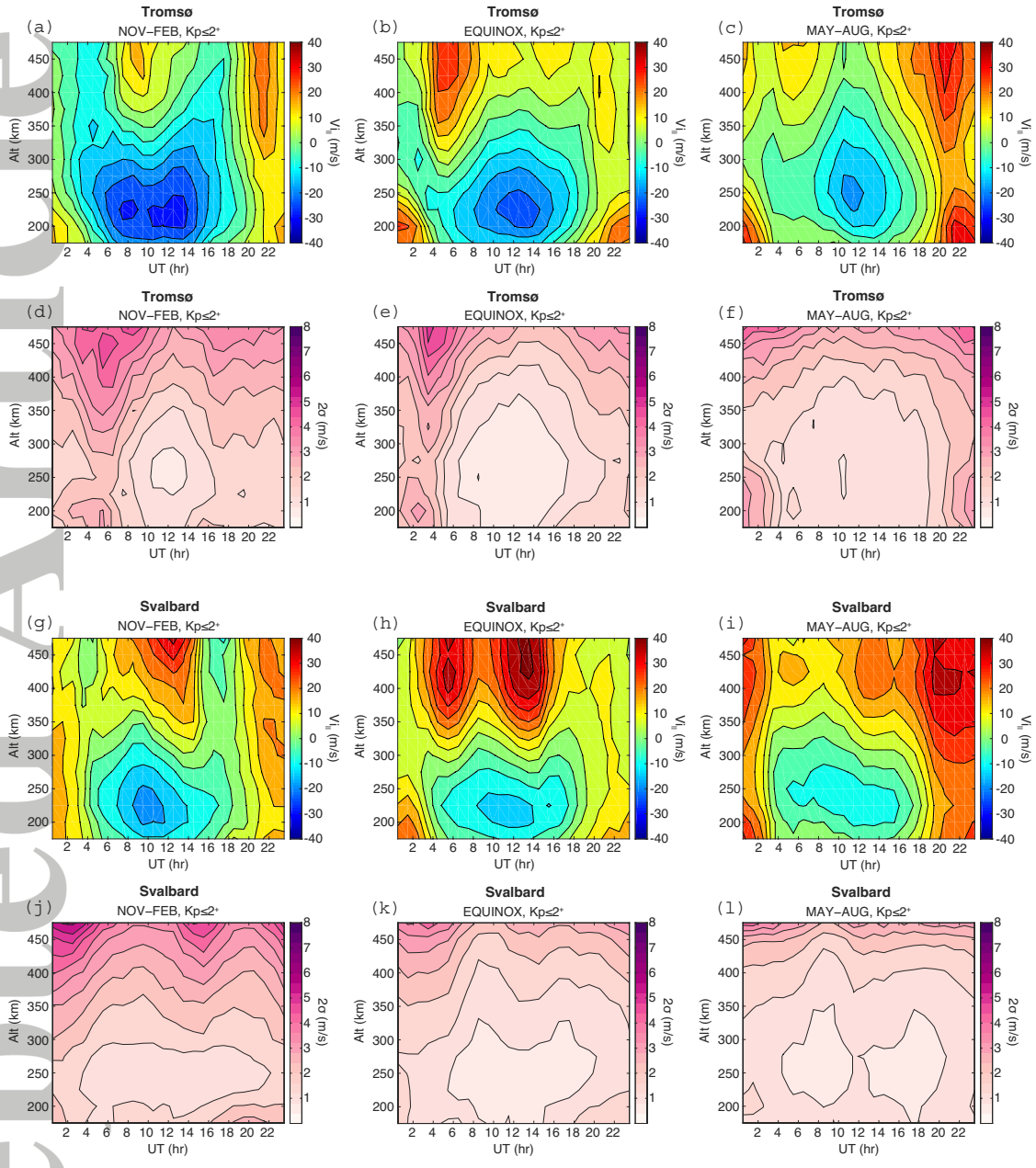

Figure 4. The dependence of the average field-aligned ion velocity (positive upward) on season for (a–c) for Tromsø and (g–i) for Svalbard. 2σ errors are shown in (d–f) for Tromsø and in (j–l) for Svalbard. The average standard deviations are 33.2, 28.7, and 21.1 m/s for (a), (b), and (c), respectively; and 46.2, 35.0, and 27.1 m/s for (g), (h), and (i), respectively. The average 2σ errors are 2.37, 1.89, and 2.01 m/s for (a), (b), and (c), respectively; and 2.39, 1.61, and 1.48 m/s for (g), (h), and (i), respectively.

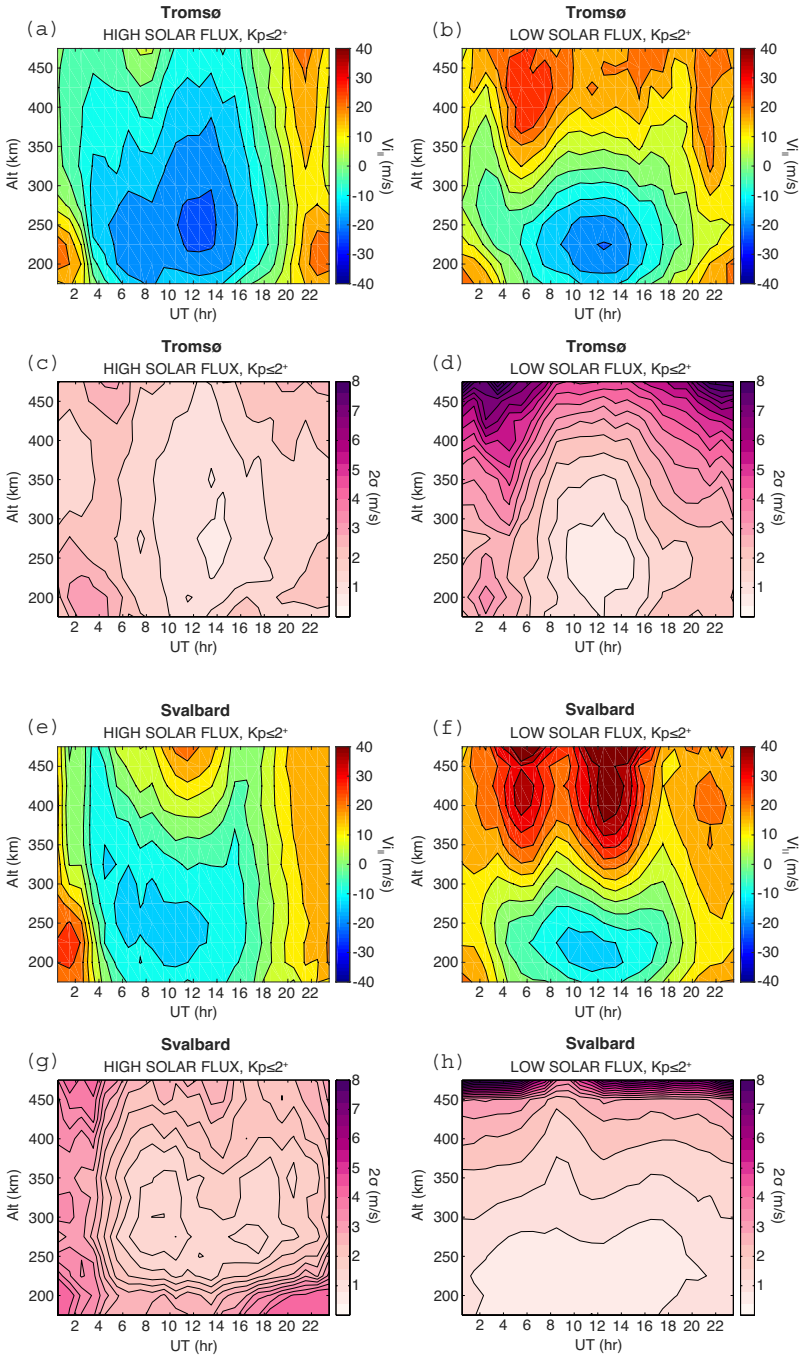

Figure 5. The dependence of the average field-aligned ion velocity (positive upward) on solar activity (a, b) for Tromsø and (e, f) for Svalbard. 2σ errors are shown in (c, d) for Tromsø and (g, h) for Svalbard. The average standard deviation is 21.7 and 35.5 m/s for (a) and (b), respectively; and 34.1 and 38.7 m/s for (e) and (f), respectively. The average 2σ error is 1.83 and 3.14 m/s for (a) and (b), respectively; and 2.44 and 2.02 for (e) and (f), respectively.

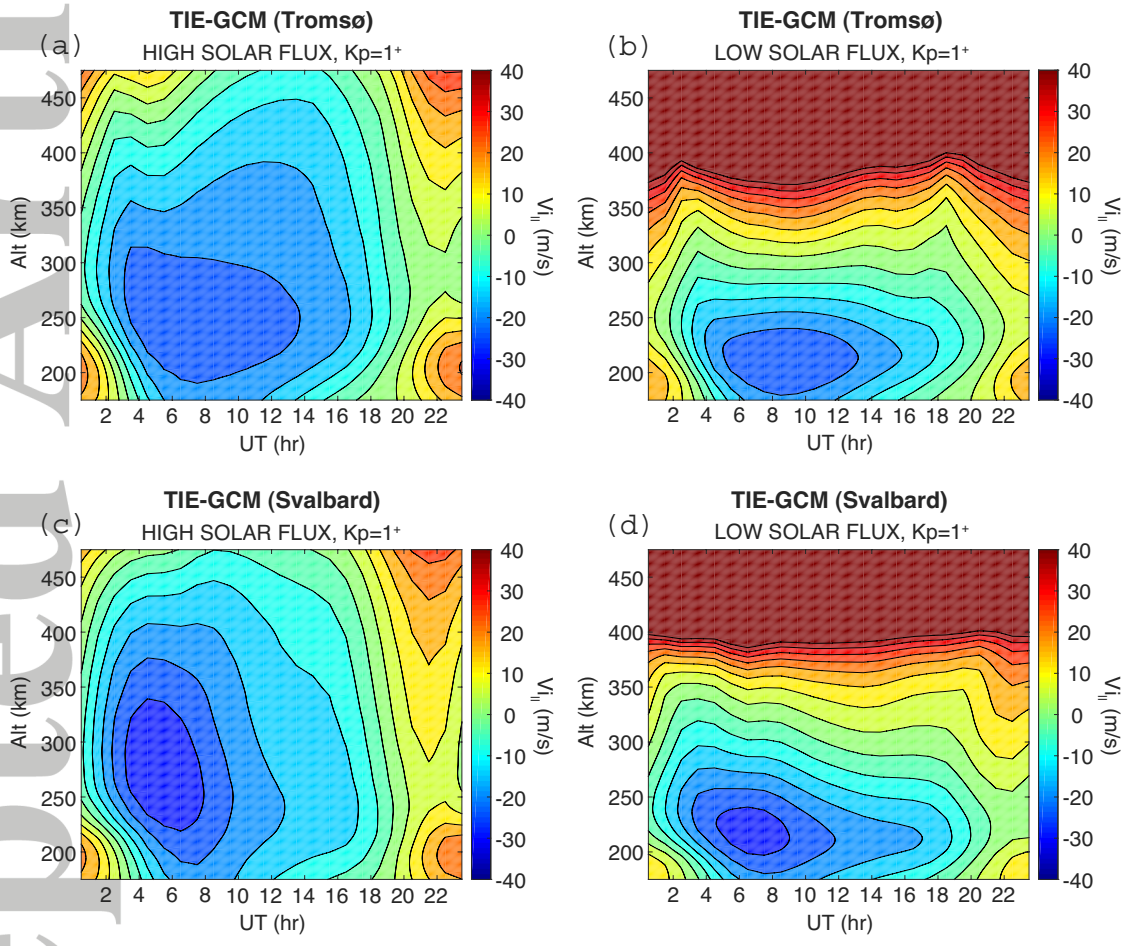

Figure 6. The dependence of the TIE-GCM field-aligned ion velocity (positive upward) on solar activity for (a, b) for Tromsø and (c, d) for Svalbard.

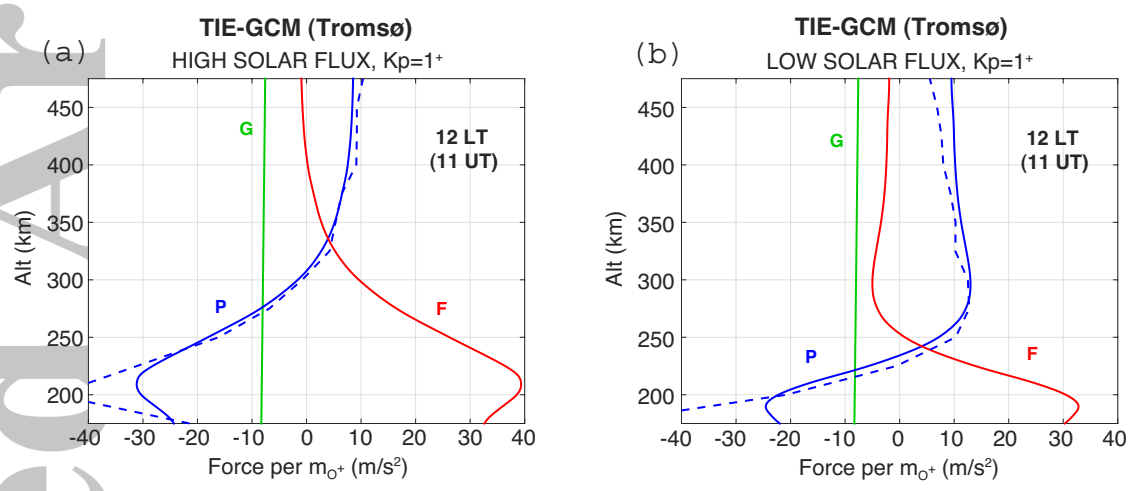

Figure 7. Altitude profiles of the ion-neutral frictional force (**F**), gravity force (**G**), and plasma pressure gradient force (**P**) at 1200 LT over Tromsø, derived from the TIE-GCM for (a) high and (b) low solar flux conditions. The plasma pressure gradient force derived from the Tromsø radar data is also indicated by the dashed lines.

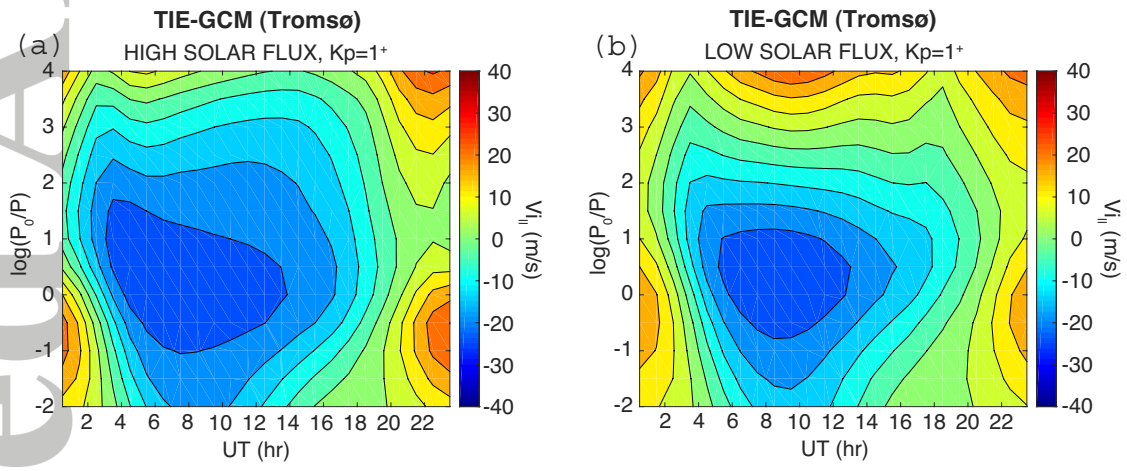

Figure 8. Same as Figures 6a and 6b except that the results are presented in the log-pressure coordinate system.

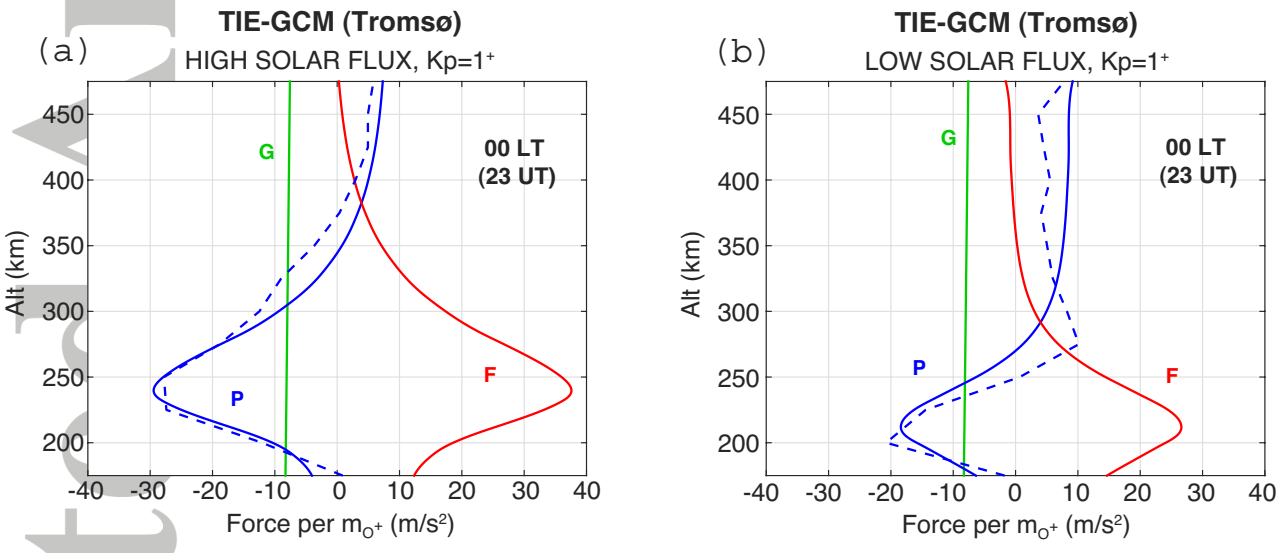

Figure 9. Same as Figure 7 except for 0000 LT.

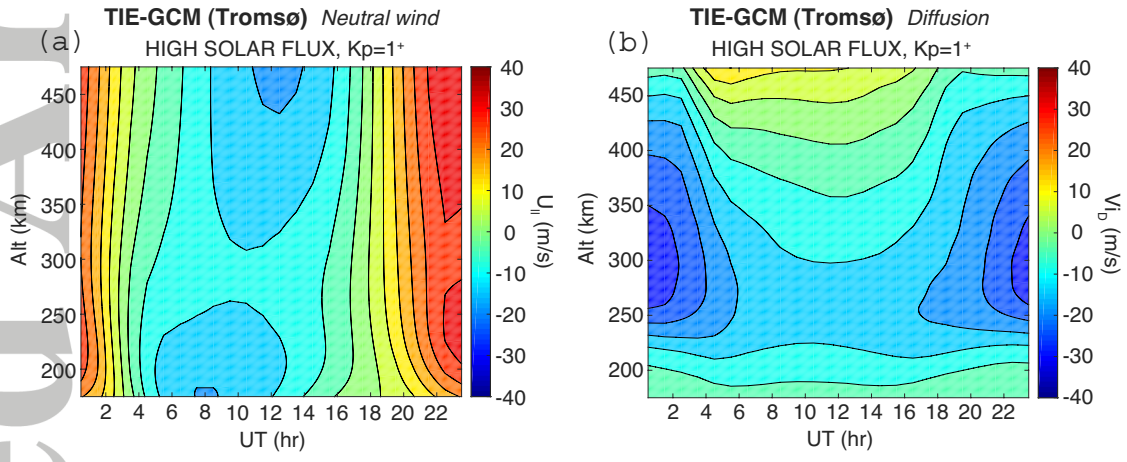

Figure 10. (a) The field-aligned neutral wind velocity (i.e., the field-aligned projection of the horizontal wind) and (b) the ambipolar diffusion velocity over Tromsø, derived from the TIE-GCM. The corresponding results for the field-aligned ion velocity can be found in Figure 6a.